Available online at www.sciencedirect.com

jmr&t Journal of Materials Research and Technology

https://www.journals.elsevier.com/journal-of-materials-research-and-technology

Original Article

Effect of MAG welding transfer mode on sigma phase precipitation and corrosion performance of 316L stainless steel multi-pass welds

L.H. Guilherme[a,*], A.V. Benedetti[c], C.S. Fugivara[c], R. Magnabosco[d], M.F. Oliveira[b]

[a] Engineering Department, Soudap Engineering Company, Araraquara, SP, Brazil
[b] Materials Engineering Department, São Carlos School of Engineering, University of São Paulo (USP), São Carlos, SP, Brazil
[c] Chemistry Institute, São Paulo State University (UNESP), Araraquara, SP, Brazil
[d] Materials Engineering Department, University Centre of FEI (FEI), São Bernardo do Campo, SP, Brazil

ARTICLE INFO

Article history:
Received 4 February 2020
Accepted 11 July 2020
Available online 7 August 2020

Keywords:
AISI 316L
Welding
MAG metal transfer modes
Pitting corrosion
Sigma phase
Heat-exchangers

ABSTRACT

The effect of multi-pass MAG welding transfer modes on the sigma phase precipitation and corrosion performance of AISI 316L thick plate were investigated. The evolution of the microstructure was examined by optical and electron microscopy as well as ferritscope measurements and energy dispersive X-ray spectrometry. An electrochemical microcell was then used to characterize the electrochemical behaviour of the different weld regions. The fusion line was the most critical zone for pitting corrosion for all welding procedures, due to the sigma phase precipitation, alloy elements partitioning and galvanic coupling between base metal and weld metal. It was observed the formation of sigma phase after short-circuiting or spray-arc modes, with no evidence of it to the pulsed-arc, which obtained the best corrosion resistance performance. The results evidenced the selective corrosion around sigma phase due to the depletion in Cr and Mo, with subsequent pitting nucleation. A strong correlation between the MAG welding transfer modes and the sigma phase morphology was observed. The influence of weld parameters on microstructure evolution and corrosion resistance performance was discussed. The corrosion resistance performance of the MAG welding procedures was ranked as: pulsed-arc > short-circuit > spray-arc.

© 2020 The Authors. Published by Elsevier B.V. This is an open access article under the CC BY-NC-ND license (http://creativecommons.org/licenses/by-nc-nd/4.0/).

1. Introduction

Stainless steels are widely used in beverage, food, pharmaceutical, cosmetic and chemical industries, as well as in oil and gas refineries due to their good resistance to corrosion and oxidation, mechanical strength at high temperatures, weldability and relative low cost [1–6].

The gas metal arc welding process (GMAW) also known by its subtypes processes, metal inert gas (MIG) and metal active gas (MAG), basically produces metallic droplets, from a consumable wire, which are transferred through an electric arc to a welding pool on the workpiece (base metal). The different transfer behaviours, referred to as metallic transfer modes, can be influenced by the composition and diameter of the consumable wire, shield gas composition, arc length and the electric current [7,8].

The natural transfer modes, such as short-circuit and spray, occur as a function of the electrical parameters (voltage

* Corresponding author.
E-mail: lh.guilherme@soudap.com.br (L. Guilherme).
https://doi.org/10.1016/j.jmrt.2020.07.039
2238-7854/© 2020 The Authors. Published by Elsevier B.V. This is an open access article under the CC BY-NC-ND license (http://creativecommons.org/licenses/by-nc-nd/4.0/).

and current). The short-circuit mode needs a contact (short-circuit) between the droplet under formation and the pool before drop detachment, and the arc is extinguished during the short-circuit periods, operating in medium heat input. The spray transfer mode is characterized by small droplets (close to the electrode diameter) transferring from the electrode tip to the weld pool at a rate of hundreds per second, without short-circuiting the pool. The heat transfer to the pool is regular and in high levels. On the other hand, there are the controlled transfer modes, such as pulsed arc, which uses a long arc length and the welding current is cyclically pulsed from a low value (base current). This is sufficient, however, to maintain the arc, to a high and sufficient value pulse current to form and detach a droplet (a spray-like transfer), resulting in a low heat input [7]. Each metallic transfer mode has a specific heat input corresponding to the configuration of the welding process [9] which, in turn, influences the microstructure evolution of the weld metal in stainless steels [10,11].

After solidification of the weld metal of an AISI 316L alloy, basically a biphasic microstructure composed of austenite (γ) and delta-ferrite (δ-ferrite) was formed. The volumetric fraction of each phase depends on factors such as equivalents of chromium (Cr_{eq}) and nickel (Ni_{eq}) in the base and filler metals as well as the alloying dilution obtained in the procedure and the final Cr_{eq}/Ni_{eq} ratio in the weld [12,13]. It should be noticed that the multi-pass welding of the AISI 316L alloy can cause sigma phase formation by the eutectoid decomposition to delta-ferrite ($\delta \rightarrow \sigma + \gamma_2$) or by nucleation and growth from delta-ferrite. Sigma phase is harmful for the corrosion resistance [14–19]. A Cr and Mo depleted zone appears surrounding sigma phase, usually secondary ferrite or austenite [16], which locally reduces the pitting potential [20], leading to a selective corrosion and subsequent preferential dissolution of one phase [20–27]. The chemical composition of sigma phase for the 316L stainless steel was quantified (wt. %) as 55% Fe, 29% Cr, 5% Ni and 11% Mo [15].

Electrochemical studies of corrosion at localized regions are possible with the use of electrochemical microcells, where the exposed surface area is drastically reduced. Numerous publications have demonstrated the operation, advantages and limitations of electrochemical microcells in the study of various systems [28–38], including studies of microregions of welded joints [30,39–41]. The advantage of the microcell for the study of multi-pass welding should be noticed, since the electrochemical behaviour can be evaluated as a function of the microstructure of each microregion of the joint [30].

The localized corrosion in equipment of stainless steel is a common problem in industrial sites, such as citric, biochemical, and chemical. Previous studies have investigated the influence of sigma phase in the corrosion resistance [12,26], and the corrosion performance of different weld microregions [40]. However, there are no researches that have investigated the corrosion performance of AISI 316L weld microregions produced by distinct MAG transfer modes, classifying the best welding procedure based on corrosion performance.

Therefore, the present work investigated the correlation between MAG welding procedures, the precipitated sigma phase morphology, and the corrosion resistance performance of weld regions in AISI 316L stainless steel aiming the improvement of welding procedures. The welding was performed by the MAG process with the natural metal transfer as short-circuit and spray-arc, and with controlled metal transfer, pulsed-arc [7]. Scanning electron microscopy (SEM) in the backscattered electrons (BSE) mode was used to identify the sigma phase as well as the microstructure of the welded joint. Cyclic potentiodynamic polarization tests with a microcell were conducted on the AISI 316L stainless steel in specific weld regions until it exceeded the pitting potential (E_{pit}). Moreover, potentiostatic etching tests were conducted in the window of passive anodic behaviour to allow microstructural evaluation of the wetted area prior to the pitting nucleation. The microstructure of the scanned surface area was also evaluated by SEM after the electrochemical corrosion tests.

2. Experimental procedure

The AISI 316L stainless steel plate with a thickness of 15.80 mm was used as the base metal, and the AWS ER316L solid wire with a diameter of 1.2 mm was used as filler metal. Table 1 shows the chemical composition of the base and filler metals which were obtained by atomic absorption spectrometry (AAS) and X-ray fluorescence (XRF) spectrometry. It is important to point out that the chemical specification of base metal and filler metal are in accordance with the ASTM A-240 and ASME section II SFA-5.9, respectively. The Cr_{eq}/Ni_{eq} ratio was calculated according to Delong Eqs. (1) and (2) and compared with the Schaeffler's diagram [12,13].

$$Cr_{eq} = \%Cr + \%Mo + 1.5\%Si + 0.5\%Nb \quad (1)$$

$$Ni_{eq} = \%Ni + 30\%C + 30\%N + 0.5\%Mn \quad (2)$$

According to the literature, the solidification mode of austenitic stainless steel weld metal can result in a monophasic microstructure or in a biphasic microstructure composed of austenite and ferrite phases, as it can be predicted based on the chemical composition and weld dilution. The solidification mode can occur with the fully austenitic [A], or with the austenite as the primary (leading) phase [AF mode], or delta-ferrite as the primary phase [FA mode] or fully ferritic [F mode]. The transition from AF mode to F mode occurs through

Table 1 – Chemical compositions of the base and filler metals and respective equivalents of Cr and Ni.

Sample	Elements (wt. %)											
	C	Cr	Ni	Mo	Mn	P	S	Si	Al	Cu	Cr_{eq}	Ni_{eq}
SA-240-316L	0.02	18.14	8.1	2.0	1.3	0.036	0.001	0.4	0.01	0.09	20.74	9.35
AWS ER 316L	0.02	18.79	11.2	2.5	1.6	0.023	0.015	0.7	–	0.06	22.34	12.60

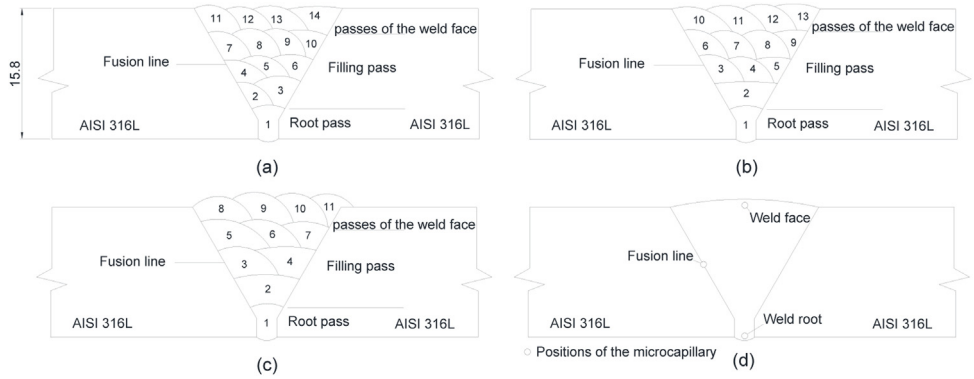

Fig. 1 – Schematic illustration showing the weld passes for each of the transfer modes: (a) short-circuit, (b) pulsed arc, (c) spray arc; and (d) weld regions where the microcell was coupled for the electrochemical tests.

a change in the Cr_{eq}/Ni_{eq} ratio [14], as can be seen from Eqs. (3)–(6):

$$L \rightarrow (L+\gamma) \rightarrow \gamma \quad \text{[A mode]} \tag{3}$$

$$L \rightarrow (L+\gamma) \rightarrow (L+\gamma+\delta) \rightarrow (\gamma+\delta) \quad \text{[AF mode]} \tag{4}$$

$$L \rightarrow (L+\delta) \rightarrow (L+\delta+\gamma) \rightarrow (\gamma+\delta) \quad \text{[FA mode]} \tag{5}$$

$$L \rightarrow (L+\delta) \rightarrow \delta \quad \text{[F mode]} \tag{6}$$

where, L is the liquid phase, γ is austenite and δ is delta-ferrite, respectively.

Three different multi-pass welded samples were manufactured by the automatic MAG process using the short-circuit, spray-arc and pulsed-arc transfer modes in the flat position (1G). Also, by using a single V groove and the one-side welding technique. This automatic welding process was performed using an ESAB AristoMig 4004i Pulsed machine. The amount and sequence of passes are schematized in Fig. 1. The weld regions were classified as weld face, weld root and fusion line to systematize the microstructural observations and electrochemical tests; each specific area can be seen in Fig. 1(d). An argon–oxygen gas mixture was used as shield gas with a composition of 98% Ar + 2%O_2 with a flux of 20 L/min. The parameter CTWD represents the distance from the end of the contact tip to the work piece, and it is smaller for the short-circuit because the welding wire makes physical contact with the base material. On the another hand, larger CTWD distances are required to the pulsed-arc and spray-arc to create and transfer tiny molten droplets across the arc [7].

The macroscopic analysis was conducted to evaluate the chemical composition of weld metals by calculating the dilution percentage ($\%D_L$) of base metal. The estimation of total area of fusion zone (A_{FZ}), the area of top (A_{TR}) and root (A_{RR}) reinforcement were found out using Autocad 2016 software. The area of weld root gap (A_{WA}) was estimated based on the weld joint geometry, as schematically shown in Fig. 2. The $\%D_L$ was calculated according to the following equations [42]:

$$A_{WA} = A_{WA1} + 2A_{WA2} + A_{TR} + A_{RR} \tag{7}$$

$$A_{BM} = A_{FZ} - A_{WA} \tag{8}$$

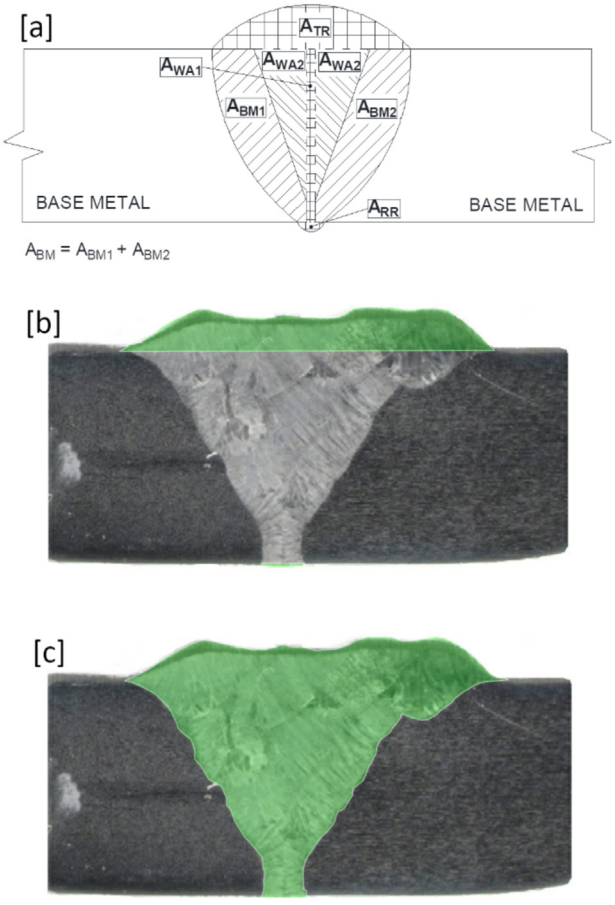

Fig. 2 – Schematic view of different locations of welded joint considered in graphical measurement for dilution calculation (a) classification of each area of welded joint, (b) top and root area of weld calculated using Autocad software and (c) area of weld fusion zone calculated using Autocad software.

$$\%D_L = \frac{A_{BM}}{A_{FZ}} = \frac{A_{FZ} - A_{WA}}{A_{FZ}} \tag{9}$$

The average dilution was measured macroscopically by the area of the welding bed relative to the initial joint profile at

Table 2 – Welding conditions to the short-circuit arc transfer mode.

Weld pass	Welding current (A)	Welding voltage (V)	Travel speed (mm/min)	Heat input (kJ/mm)	Width of weld (mm)
Root	$180^{\pm3}$	$19.3^{\pm0.1}$	$202^{\pm1}$	$1.0^{\pm0.1}$	$4^{\pm0.2}$
2–10	$200^{\pm4}$	$20.8^{\pm0.1}$	$205^{\pm2}$	$1.2^{\pm0.2}$	$5^{\pm0.4}$
11–14	$190^{\pm2}$	$20.5^{\pm0.1}$	$210^{\pm1}$	$1.1^{\pm0.1}$	$5^{\pm0.2}$
Contact tip to work distance (CTWD): 10 mm.					

Table 3 – Welding conditions to the pulsed-arc transfer mode.

Weld pass	Welding average current (I_a)	Welding voltage (V)	Travel speed (mm/min)	Heat input (kJ/mm)	Width of weld (mm)
Root	$130^{\pm1}$	$25.1^{\pm0.1}$	$305^{\pm.2}$	$0.6^{\pm0.2}$	$5^{\pm0.1}$
2–9	$145^{\pm2}$	$26.5^{\pm0.1}$	$292^{\pm2}$	$0.8^{\pm0.3}$	$5^{\pm0.2}$
10–13	$140^{\pm2}$	$25.3^{\pm0.1}$	$302^{\pm2}$	$0.7^{\pm0.2}$	$5^{\pm0.2}$
CTWD: 15 mm.					

Table 4 – Welding conditions to the spray-arc transfer mode.

Weld pass	Welding current (A)	Welding voltage (V)	Travel speed (mm/min)	Heat input (kJ/mm)	Width of weld (mm)
Root	$280^{\pm3}$	$32.5^{\pm0.1}$	$354^{\pm.2}$	$1.6^{\pm0.2}$	$6^{\pm0.2}$
2–7	$320^{\pm6}$	$34.8^{\pm0.1}$	$351^{\pm2}$	$1.9^{\pm0.3}$	$7^{\pm0.5}$
8–11	$300^{\pm5}$	$34.5^{\pm0.1}$	$370^{\pm2}$	$1.7^{\pm0.2}$	$6^{\pm0.3}$
CTWD: 20 mm.					

the cross section of the samples. The results for each transfer mode were: 32% to the short-circuit, 42% to the spray, 24% to the pulsed. The heat input was calculated using ASME IX [43] in Eq. (10) by dividing the average power (current × voltage) by the travel speed (mm/s). In order to calculate the heat input to the pulsed transfer mode, the average current (I_a) of this process was determined, correlating the currents of peak (I_p) and base (I_b) to the relative time of each current during welding process, defined as pulse time (t_p) and base time (t_b), as can be seen in Eq. (11) [44]. It is worth highlighting that the maximum interpass temperature was 150 °C for the multi-pass welding. The details of the welding parameters of each MAG transfer mode are summarized in Tables 2–4.

$$E = \frac{U.I.60}{v} \tag{10}$$

where: "E" is the heat input in kJ/mm, "U" is the welding voltage in volts, "I" is the welding current in amperes and "v" is the travel speed in mm/s.

$$I_a = \frac{(I_p t_p + I_b t_b)}{(t_p + t_b)} \tag{11}$$

where: "I_a" is the average current, "I_p" is the peak current, "I_b" is the base current, "t_p" is the relative time in the peak current and "t_b" is the relative time in the base current. The unit of all current quantities are in amperes.

Based on chemical analysis of the base metal and filler metal, Eqs. (1) and (2) were applied to determine their equivalents of Cr and Ni (Cr_{eq} and Ni_{eq}), which were related to the dilution rate of each MAG transfer mode in order to provide the respective equivalent of the welded joints. Based on the Cr_{eq}/Ni_{eq} ratio of welded joints, the solidification mode and the ferrite number (Delong diagram) was presumed [12]. Also, the volumetric fraction of delta-ferrite was measured with a Fischer MP3 ferritscope to the base metal, weld face, weld root and fusion line.

For microstructural observation, the samples were polished in a semi-automatic Buehler Automet 250 polisher with alumina of different grain sizes down to 0.05 μm. The samples were ultrasonically cleaned in water for 5 min; the polishing agent was changed every time. The weld zone was etched with aqua-regia during 2 min for microstructural analysis by optical microscopy and scanning electron microscopy (SEM). In order to identify the precipitated sigma phase in the weld metal, a FEG-SEM JEOL JSM-7500F microscope equipped with a PC-SEM v.2.1.0.3 analyser was used to take backscattered electron (BSE) images of the polished surface (without etching). The chemical analysis of the sigma phase was performed by energy-dispersive X-ray spectroscopy (EDS). The local chemical composition can be changed between weld microregions and this condition generates susceptibility to localized corrosion in welded joints [45]. The local chemical composition variations of austenite and ferrite phases were investigated by EDX analysis for the weld microregions: weld face, weld root and fusion line. The EDX data were acquired using an 80 mm^2 X-Max detector, collecting 10^6 counts in each point, and the EDX spectra were quantified using ZAF correction in Aztec software. For each phase (austenite and ferrite), five (5) spectra were acquired for each one of microregions.

An electrochemical microcell, as describe elsewhere [46], based on a microcapillary with a diameter of 500 μm (~0.002 cm^2), and composed of three electrodes, was used: a platinum counter electrode, a silver|silver chloride|3 mol L^{-1} potassium chloride (Ag|AgCl|KCl 3 mol L^{-1}) reference electrode and the sample as working electrode. Cyclic potentiodynamic polarization (CPP) tests were performed in 3.5% NaCl aqueous solution by applying flow with drip control and average

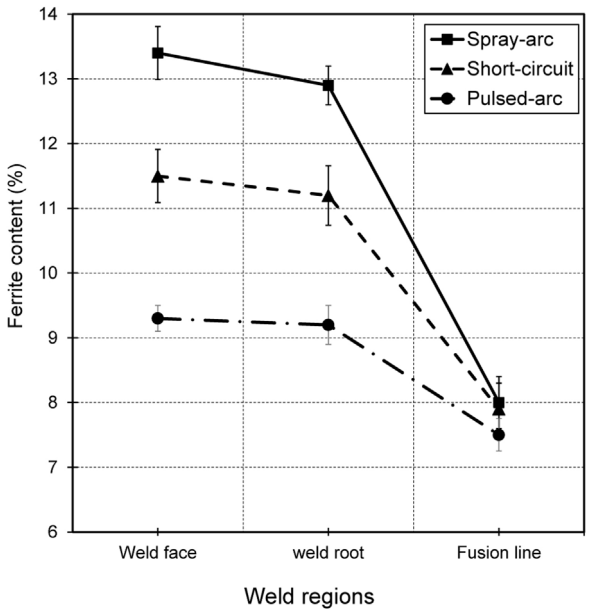

Fig. 3 – Quantitation of ferrite content on the weld regions of short-circuit, spray-arc and pulsed-arc. The error bars are standard deviation of 10 measurements by ferritscope.

flow rate of 1 drop per second (~50 μL/s) at 25 °C. A Palmsens PSTrace-3 potentiostat was used for tests. After the OCP stabilization (5 min), an anodic polarization scan was performed at a sweep rate of 1.67 mV s^{-1}. The anodic scan was reversed at a current density of 1 mA cm^{-2} with the sample being then scanned in the cathodic direction to a potential of −200 mV *vs.* OCP. The weld microregions inspected by CPP tests were the base metal, weld face, weld root, and fusion line. Fig. 1(d) shows the coupling position of the microcapillary on weld microregions and it is highlighted that five measurements were made in each microregion.

Potentiostatic etching was performed in weld root region with the presence of sigma phase to assess its effect at the electrochemical behaviour. These microregions were identified by SEM BSE mode and the coordinates were used to track back its positions and execute the local electrochemical tests. An etching potential 400 mV *vs.* Ag|AgCl|KCl 3 mol L^{-1} was used for 10 min in 3.5% NaCl aqueous solution. This procedure allowed a better understanding regarding the influence of the microstructure on the electrochemical behaviour of the welded joint at potentials prior to the pitting potential.

The electrochemical behaviour was evaluated in terms of the corrosion potential (E_{corr}), pitting potential (E_{pit}), repassivation potential (E_{rp}), passive region (E_{rp}–E_{corr}) and in combination with microstructure observation by SEM after the CPP measurements and potentiostatic etching.

3. Results and discussion

Fig. 3 shows the results of the delta-ferrite measurement with a ferritscope in the weld regions: face, root, and fusion line. It is highlighted that at the base metal, AISI 316L, there was no evidence of the remaining ferrite.

The presence of delta-ferrite in the weld metal corroborates the supposition about the FA solidification mode predicted by the calculation of the ratio $(Cr/Ni)_{eq}$ and proposed in the literature [12,13], stating that such solidification mode happens for $1.5 < Cr_{eq}/Ni_{eq} < 2.0$. The solidification mode of the weld metal was supposed as ferritic–austenitic (FA), according to Eq. (5), for all transfer modes based on the Cr_{eq}/Ni_{eq} ratio and the results presented in Table 5. In this solidification mode, the ferrite, with dendritic morphology, is the primary phase, and the austenite is later formed at the ferrite/liquid interface [14]. According to Table 5, the quantification of the Cr_{eq}/Ni_{eq} ratio shows the tendency of pulsed-arc transfer mode to present lower ferrite fraction in the weld microstructure, and the higher ferrite fraction was observed in spray-arc welding. The short-circuit provided an intermediate result.

A typical microstructure for the welded joint can be observed in Fig. 4, highlighting the transition on the fusion line of austenitic base metal to the dual-phase weld metal (Fig. 4(a)), which was represented by the equiaxed grains of the face-centred cubic (FCC) arrangement of the base metal towards the weld metal. This presented the ferrite as dendritic morphology surrounded by austenite bands (Fig. 4(b)). Despite the same solidification mode presented by all MAG transfer modes, it is noteworthy that the difference in the Cr_{eq}/Ni_{eq} ratio influenced the interaction between the austenite bands and ferrite dendrites [13]. For the lower Cr_{eq}/Ni_{eq} ratio (1.6), pulsed-arc transfer mode, relatively large austenite bands and fine ferrite was observed. On the other hand, the spray-arc transfer mode showed the biggest Cr_{eq}/Ni_{eq} ratio (1.9) and consequently it was characterized by narrow austenite bands with large ferrite.

The chemical composition of austenite and ferrite within the welded regions were measured by EDS, as describe elsewhere [45], and the compositional differences caused by local element segregations were evaluated. The elemental compositions of the different weld regions and differences in austenite and ferrite are summarised in Table 6, with the data interpreted using the pitting resistance equivalent number (PREN) calculations, according to Eq. (12), and the results are shown in Fig. 5. The PREN is a predictive measurement of a stainless steel resistance to localized pitting corrosion based on its chemical composition, and the delta/gamma (δ/γ) PREN ratio can demonstrate the susceptibility to the galvanic interaction between austenite and ferrite, where the higher ratio indicates the most susceptibility. The corrosion performance for dual phase stainless steel, such as AISI 316L weld microstructure, is defined by PREN of ferrite phase (weak phase). However, it is important to consider the PREN of austenite phase in corrosion performance analysis due to the galvanic interaction [45,47].

$$PREN = \%Cr + 3.3\%Mo + 16\%N \quad (12)$$

The weld face of all MAG transfer modes presented a regular PREN for austenite and ferrite, clearly represented by single pass weld and chemical composition of the weld consumable. The fusion line and weld root regions generated their microstructures and chemical compositions based on high dilution between base metal and weld consumable, caused by welding process, and associated with the multi-pass weld-

Table 5 – Equivalents of Cr and Ni.

Samples	Cr_{eq}	Ni_{eq}	Cr_{eq}/Ni_{eq}	Solidification mode
Spray-arc	22.0	11.5	1.9	FA
Short-circuit	22.1	12.1	1.8	
Pulsed-arc	20.5	12.8	1.6	

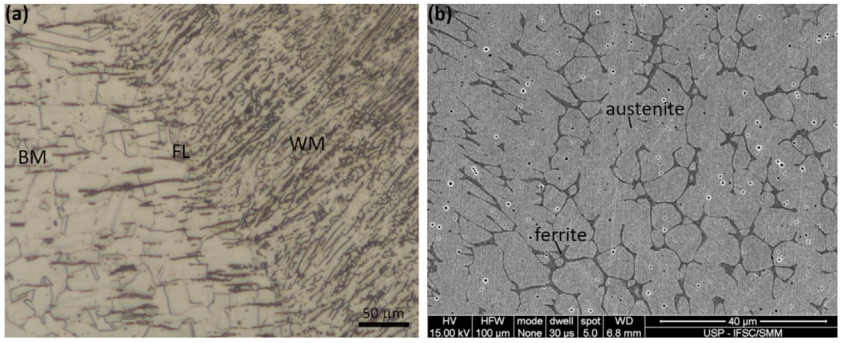

Fig. 4 – Microstructural observation of the typical welded joint showing: (a) optical microscopy of the boundary between weld metal and base metal (etched by aqua-regia), (b) SEM/BSE images to determine of austenite (light phase) and ferrite (dark phase). BM: base metal, FL: fusion line, WM: weld metal.

Table 6 – Variance in chemical composition of austenite/ferrite for the investigated weld regions.[a,b]

MAG transfer mode	Chemical composition of phases		Elements % (SD)			PREN values	PREN ratio (δ/γ)
	Region	Phase	Cr	Mo	Ni		
Short-circuit	Weld face (WF)	Ferrite	22.77 (0.15)	3.01 (<0.10)	2.82 (0.10)	32.70	1.45
		Austenite	17.36 (0.17)	1.55 (<0.10)	8.28 (0.19)	22.48	
	Fusion line (FL)	Ferrite	20.25 (0.12)	1.89 (<0.10)	2.17 (0.11)	26.49	1.32
		Austenite	16.41 (0.19)	1.11 (0.11)	7.01 (0.14)	20.07	
	Weld root (WR)	Ferrite	21.43 (0.15)	2.55 (0.12)	2.49 (<0.10)	29.85	1.41
		Austenite	16.88 (0.13)	1.29 (0.10)	7.65 (0.19)	21.14	
Spray-arc	Weld face (WF)	Ferrite	22.54 (0.20)	2.98 (0.12)	2.76 (0.12)	32.37	1.45
		Austenite	17.41 (0.19)	1.48 (<0.10)	7.99 (0.20)	22.29	
	Fusion line (FL)	Ferrite	20.01 (0.17)	1.34 (<0.10)	2.05 (<0.10)	24.43	1.22
		Austenite	16.25 (0.20)	1.12 (<0.10)	7.56 (0.18)	19.95	
	Weld root (WR)	Ferrite	21.35 (0.20)	2.41 (<0.10)	2.39 (0.10)	29.30	1.44
		Austenite	16.70 (0.11)	1.10 (<0.10)	7.32 (0.17)	20.33	
Pulsed-arc	Weld face (WF)	Ferrite	22.90 (0.14)	3.16 (0.15)	2.93 (<0.10)	33.33	1.46
		Austenite	17.45 (0.15)	1.62 (0.11)	8.22 (0.19)	22.80	
	Fusion line (FL)	Ferrite	20.43 (0.20)	2.01 (0.10)	2.09 (<0.10)	27.06	1.32
		Austenite	16.59 (0.19)	1.20 (<0.10)	7.21 (0.14)	20.55	
	Weld root (WR)	Ferrite	21.54 (0.18)	2.78 (0.12)	2.65 (<0.10)	30.71	1.43
		Austenite	16.98 (0.13)	1.35 (<0.10)	7.50 (0.13)	21.44	

[a] AISI 316L base and filler metal have no nitrogen (N) in the composition.
[b] SD = Standard deviation.

ing conditions. These conditions influenced the partitioning of alloy elements with local chemical variation and, consequently, reduced the PREN of the austenite/ferrite in these regions. As a function of the lowest dilution and heat input, the pulsed-arc mode showed the lower local chemical variation to the fusion line and weld root, corroborated by the highest PREN of ferrite and austenite, as can be seen in Fig. 5.

3.1. *Sigma (σ)-phase characterization*

The sigma phase was identified in the fusion line and weld fusion zone of the short-circuit and spray modes, and it was not observed in the pulsed-arc mode. The average size of sigma phase was 1 μm and its chemical composition was estimated by EDS, as can be seen in Table 7, corroborating the chemical composition cited in the literature [15] for the sigma phase in AISI 316L weldments. The most susceptible weld region to precipitate the sigma phase was a specific area of the weld root, due to the reheating of the root pass by the other thermal cycles of the multi-pass welding, generating a suitable time-temperature ratio to the sigma phase precipitation.

It is important to point out that the solidification mode associated with the type of the transfer mode of the MAG process exerts a significant influence on the precipitated sigma

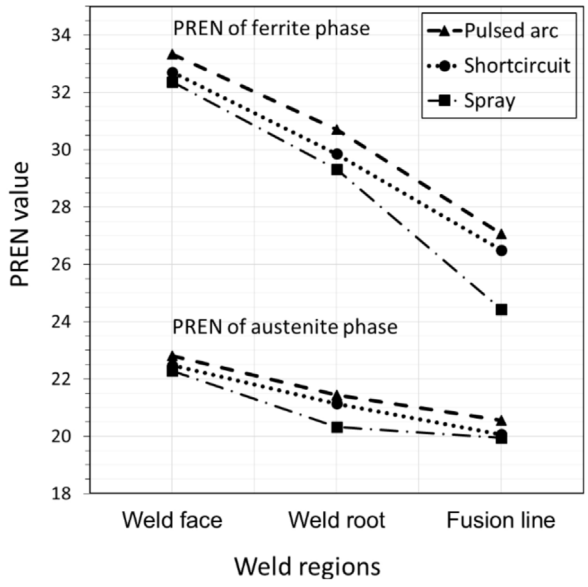

Fig. 5 – PREN values of the austenite and ferrite phases for all welding procedures.

phase morphology, as can be seen in Fig. 6. The nucleation of the sigma phase in the AISI 316L weldments was related to the FA solidification mode, where the austenite grows as a secondary phase, segregating ferritizing elements such as Cr and Mo to the liquid–ferrite interface and to the interior of the ferrite, thus enriching the austenite with Ni. Thus, the ferrite is stabilized by the segregation of Cr and Mo into the ferrite during the peritectic reaction, and these are the main forming elements of the sigma phase, hence the preferred sigma formation is always associated with the delta-ferrite [14,15]. For the spray mode, the sigma phase precipitated systematically at the gamma/delta (γ/δ) interface, surrounding the delta-ferrite (Fig. 6(a)). For the short-circuit mode, the sigma phase precipitated systematically inside the delta-ferrite (Fig. 6(b)). This difference is regarding the local partitioning of alloy elements during solidification, on solid state diffusion, and probably it can be associated with the cooling rate and phases evolution due to the specific thermal history of each MAG welding transfer mode.

The short-circuit and spray-arc transfer modes are characterized by a turbulent melt pool, a factor that intensifies the dilution of segregating elements in the liquid. However, the higher heat input of the spray-arc mode resulted in lower cooling rates and solidification, providing segregation of the alloying elements (Cr and Mo) at the gamma/delta (γ/δ) interface, resulting in sigma phase precipitation in this region. The short-circuit mode used lower heat input than spray-arc, with a consequent higher cooling rate and solidification, thus concentrating Cr and Mo inside the delta-ferrite. The time-temperature to homogeneous sigma phase precipitation is only achieved inside ferrite for the short-circuit mode. Therefore, the sigma phase precipitated inside the delta-ferrite in this later case.

For all transfer modes, the sigma phase was not detected in the base metal and did not nucleate in the weld face region, resulting on the best corrosion resistance performance to these weld regions for all assessed MAG welding procedures. This equivalent performance is related to the absence of sigma phase in the microstructure of the weld metal which, in turn,

Table 7 – Chemical composition of sigma phase for AISI 316L.

Phase	Elements (wt. %)				
	Fe	Cr	Ni	Mo	Si
Sigma (σ)	54 ± 3	28 ± 2	5 ± 1	12 ± 2	0.33 ± 0.25

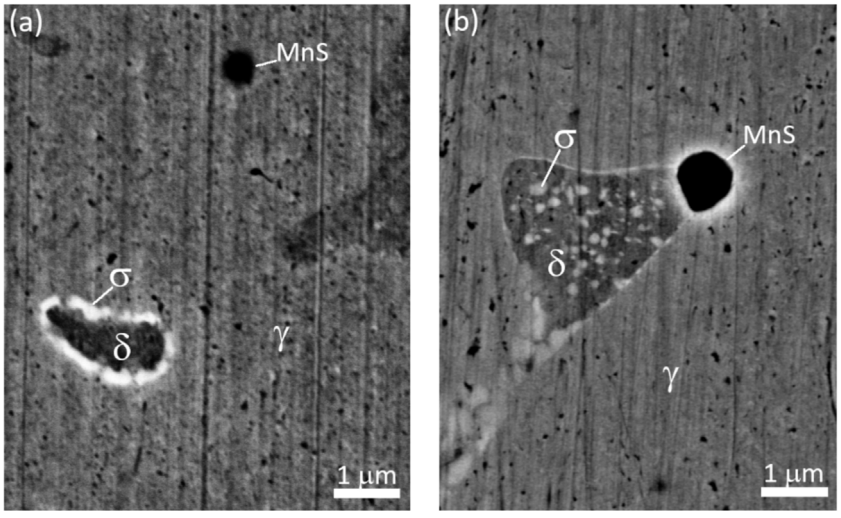

Fig. 6 – SEM/BSE micrographs showing the weld root with sigma phase precipitated to the MAG welding processes in the transfer modes of: (a) spray-arc and (b) short-circuit.

did not precipitate in the weld face, since it is the last layer of filling. Therefore, the welding pass of the face is not subjected to other thermal welding cycles, as occurs for the root pass, the most thermally affected region.

3.2. *Pitting corrosion resistance*

Fig. 7 presents the cyclic potentiodynamic polarization curves for the weld regions in 3.5% NaCl solution. All polarization curves showed a passive behaviour of the weld regions, highlighting the positive hysteresis for the fusion line regions of short-circuit and spray-arc transfer modes. The positive hysteresis occurs when reverse scan current density is greater than that for the forward scan, and it means that the passive film damage is not repaired, and pit grew after the potential was reversed. All other weld microregions showed negative hysteresis, which means that the damaged passive film repaired itself and a pit do not grow after the potential was reversed.

The PREN values of all different regions are compared to the breakdown potentials (E_{pit}) of each MAG welding procedures. The weld face region of all MAG welding procedures obtained similar corrosion resistance performance, with no evidence of pitting, and a passive region with an average potential range of 730 mV, as can be seen in CPP curves (Fig. 7(a)) and electrochemical parameters (Fig. 8). This performance was correlated to the PREN of austenite and ferrite, quantified in average values of 22.5 and 32.8, respectively, as well as the single thermal cycle to the weld face, since it is the last weld layer. The E_{pit} of the weld root regions occurred in the potential range of 440–670 mV, and it is correlated to the PREN of the phases that were relatively reduced when compared to the weld face region, and also with the changes in microstructure, which generated local Cr- and Mo-depleted zones. The microstructural evolution of the short-circuit and spray-arc transfer modes in a multi-pass MAG welding resulted in sigma phase precipitation mainly in weld root regions, and the volume fraction presents in microstructure influenced the E_{pit} of short-circuit (575 mV) and spray-arc (470 mV). The sigma phase was not evidenced in pulsed-arc microstructure and its E_{pit} (650 mV) was correlated with the PREN of ferrite (30.71). The fusion line regions were classified as critical regions for corrosion resistance performance for all MAG welding transfer modes. The worst corrosion performance was associated with the galvanic coupling between weld metal and base metal, which create a preferential site to localized corrosion [40,45,46]. In addition, it was observed a high local variation of the partitioning of alloy elements, which resulted in a significant reduction of PREN of the phases. It is important to point out that the sigma phase was generated in the fusion line region to the short-circuit and spray-arc modes, and the pitting potential was reduced due to its presence in the microstructure. For pulsed-arc, without sigma phase on its microstructure, a substantial improve in passive region quantified in 420 mV was obtained while short-circuit and spray-arc generated a passive region of 260 and 70 mV, respectively. Although without sigma phase in weld microstructure, the weld root and fusion line regions of pulsed arc obtained a reduced corrosion performance when compared to the weld face region. This performance is related to the larger dilution ratio and the greater amount of weld passes and consequent increase of weld thermal cycles.

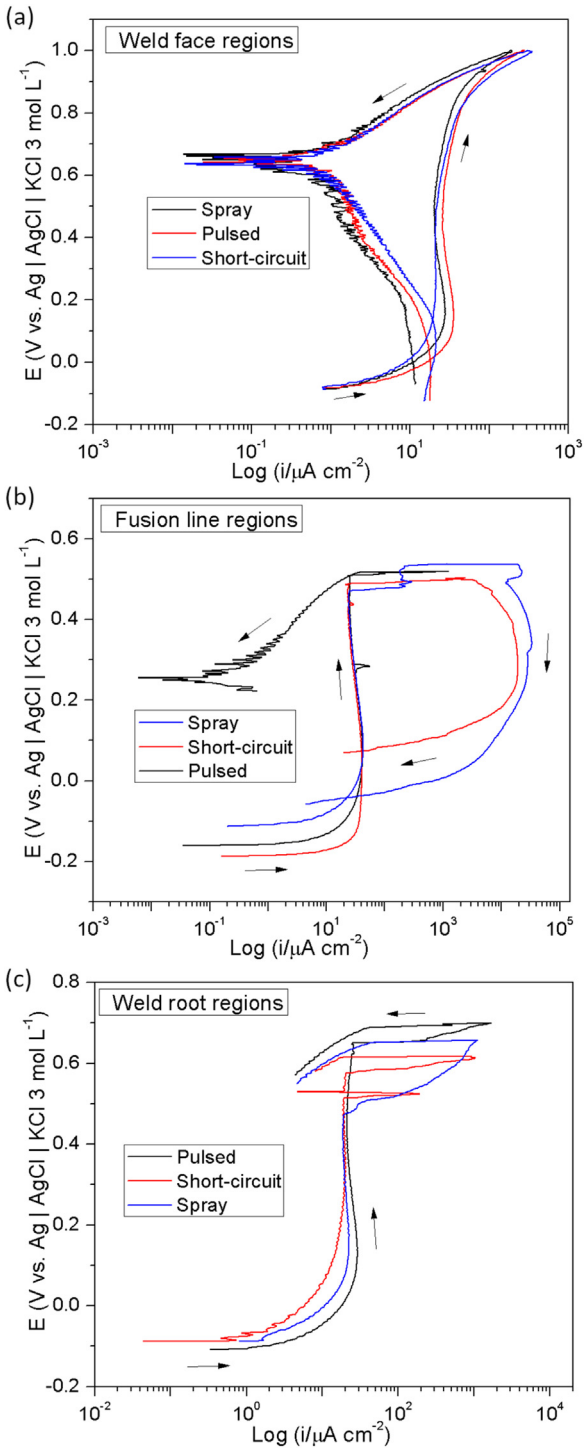

Fig. 7 – Cyclic potentiodynamic polarization curves of the MAG welding procedures comparing the weld regions: (a) weld face, (b) fusion line region and (c) weld root.

Fig. 9 shows SEM micrographs of nucleated pits at the weld root region after CPP tests in 3.5% NaCl solution, highlighting that each MAG welding transfer mode generated a specific morphology for the pitting nucleation. It is possible to observe

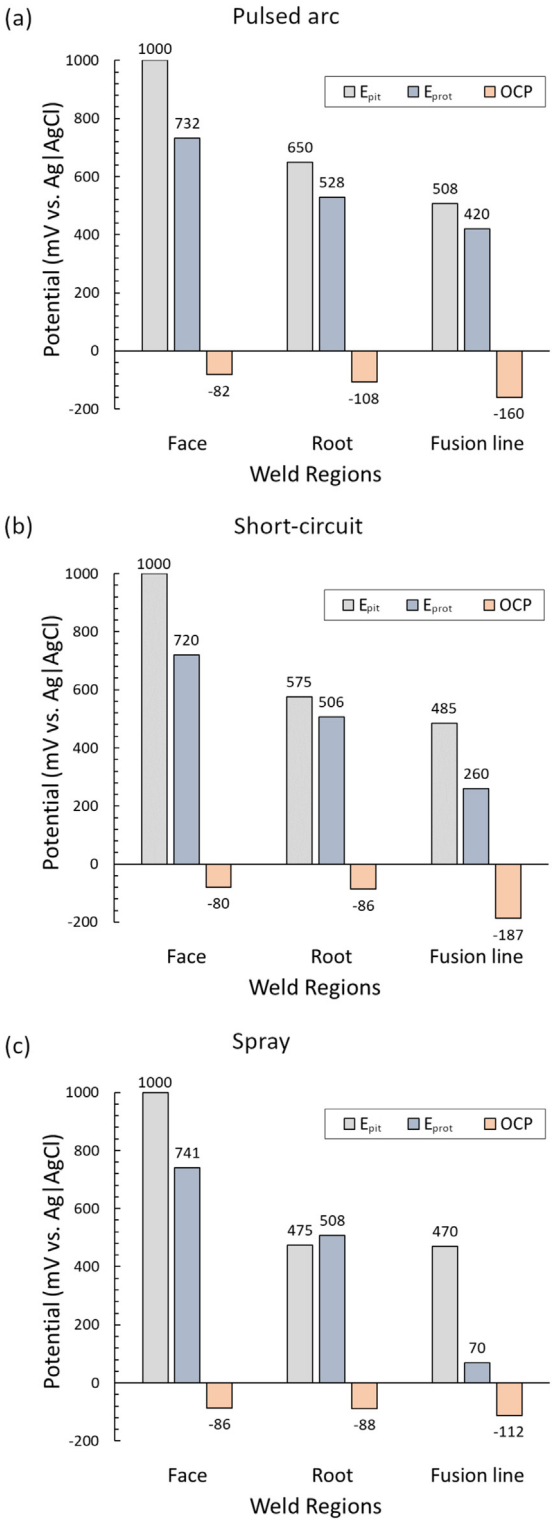

Fig. 8 – Quantitative determination of the electrochemical parameters of MAG welding procedures: (a) pulsed-arc, (b) short-circuit and (c) spray-arc.

(Fig. 9(a) and AA' view) the selective corrosion of austenite inside the pit void of the spray-arc, where the gamma/delta (γ/δ) interface created a galvanic interaction and it was preferable corroded. This is linked to the sigma phase morphology of this MAG welding transfer mode. The morphology of the short-circuit also can be linked to the sigma phase precipitation and its selective corrosion, since its edge assumes the dendritic morphology of ferrite. Therefore, it is probably that the pit nucleates in the region, where, previously, a selective corrosion of ferrite occurred. The pulsed-arc transfer mode showed a typical pitting nucleation, due to local breakdown of the passive film, with no identification of sigma phase in weld microstructure.

Fig. 10 shows the EDS spectra of the exposed surface area after polarization measurement in 3.5% NaCl solution. The EDS analysis assessed the local chemical composition of pit site (mark inside pit, Fig. 10) and non-corroded site (mark outside pit, Fig. 10) to clarify the preferable phase to corrosion. The short-circuit obtained a Cr and Mo percentage reduction of 27.4% and 54.4%, respectively, indicating that the ferrite phase was preferable corroded. On the other hand, spray-arc showed a Ni reduction of 52.2% what indicated the preferable corrosion of austenite. Therefore, the EDS analysis corroborated what the SEM micrographs indicated.

3.3. *Selective corrosion in weld root region*

The results of potentiostatic etching of weld root region of short-circuit and spray-arc at 400 mV using 3.5% NaCl solution can be seen in Fig. 11. The short-circuit mode presented selective corrosion at 400 mV, which is located before the pitting potential. This is due to the nucleation of many dispersed sigma precipitates within the ferrite (Fig. 11(a)), causing the depletion of Cr and Mo all over the ferritic matrix. Thus, selective corrosion of ferrite occurred until this phase being widely consumed, and consequently, the pitting nucleation occurred in these previous corroded regions. It is highlighted that the pitting contour presented similar morphology of the ferrite dendrite, as can be seen in Fig. 9(b), reinforcing the hypothesis that pitting nucleation occurred where the passive film was previously damaged, that is, by selective corrosion of ferrite.

Regarding the spray-arc mode, there was also a selective corrosion at 400 mV, which is inferior to the pitting potential, due to weld microstructure with precipitated sigma phase. With this welding procedure, the sigma phase was nucleated at the gamma/delta (γ/δ) interface, generating a depleted zone in this site and a galvanic interaction was established between sigma phase and austenite, which caused the selective corrosion of austenite, as shown in Fig. 11(b). Thus, this mechanism is related to the alloy elements partitioning in the gamma/delta (γ/δ) interface with sigma phase precipitation, which created a local depleted austenitic matrix, resulting in a preferable corrosion of austenite, as can be seen in Figs. 9(a) and 11(b).

4. Conclusions

The corrosion resistance performance of AISI 316L thick plate welded by distinct MAG welding transfer modes was eval-

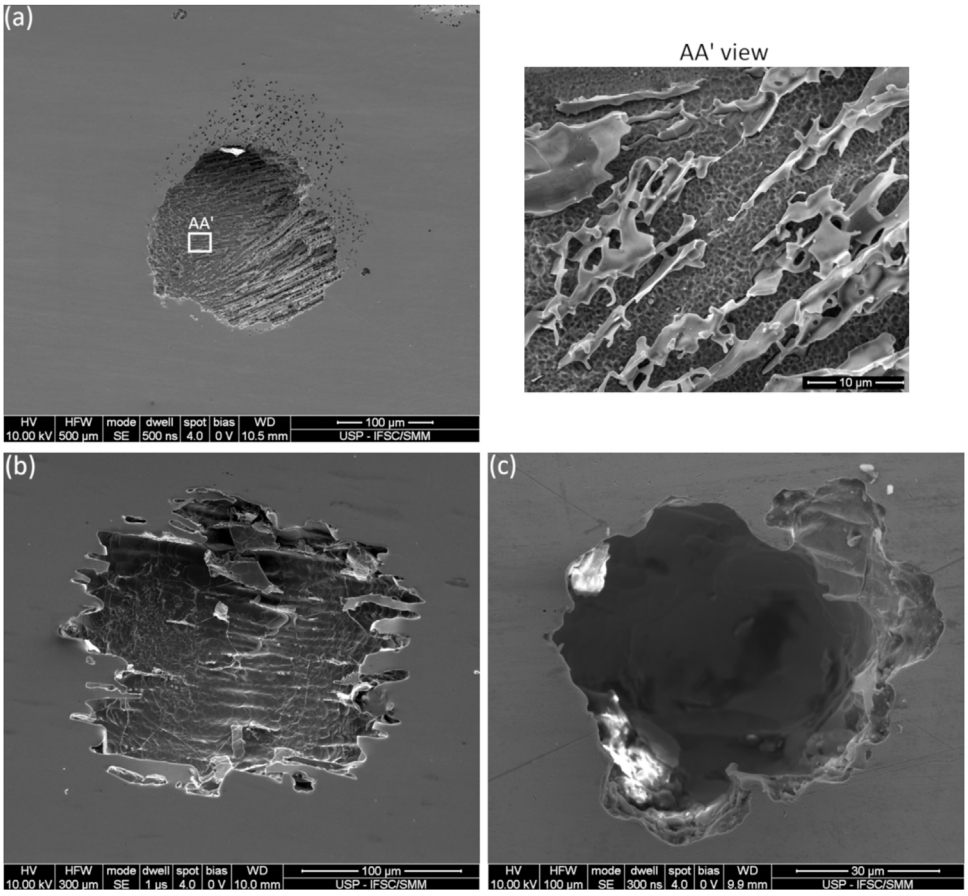

Fig. 9 – SEM micrographs of the scanned surface area of the weld root after CPP tests: (a) spray-arc with AA' view detail regarding inside of the pit, (b) short-circuit and (c) pulsed-arc.

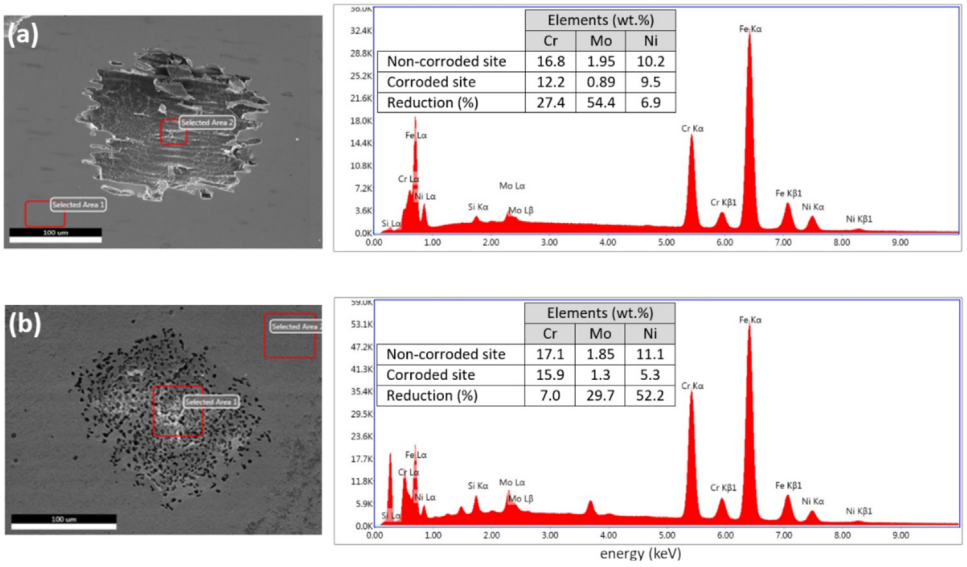

Fig. 10 – EDS analysis of the pit site and non-corroded area after polarization test in 3.5% NaCl for (a) short-circuit and (b) spray-arc.

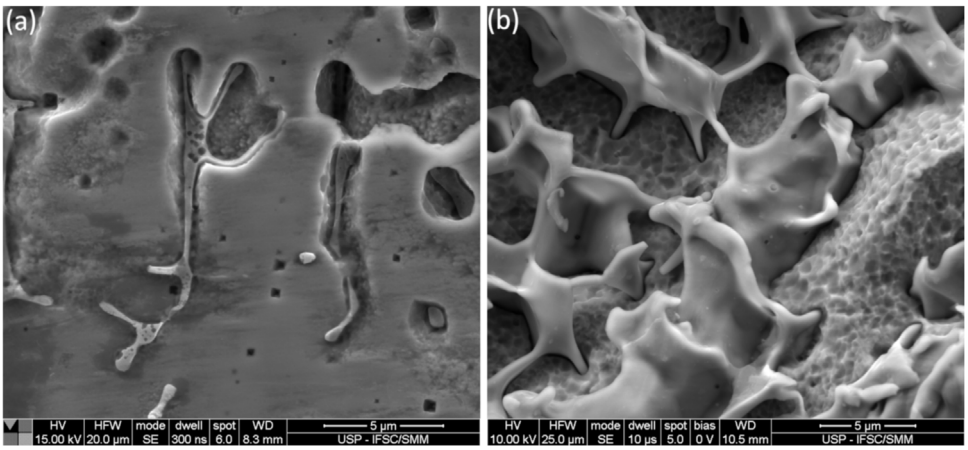

Fig. 11 – SEM micrographs of the scanned surface area after potentiostatic etching of MAG welding using: (a) selective corrosion of delta-phase due presence of the sigma-phase inside it in the short-circuit transfer mode and (b) selective corrosion of gamma-phase in the gamma/delta (γ/δ) interface due to depleted-zone caused by sigma-phase precipitation in this microregion, observed on the spray transfer mode. Electrolyte: 3.5% NaCl. Potential: 400 mV.

uated. From the results, the following conclusions can be drawn:

- The sigma phase precipitated for short-circuit and spray-arc transfer modes in the root of the welded joint, a factor attributed mainly to the welding thermal cycle of a multi-pass procedure that imposed reheating of the root pass and set up a low cooling rate.
- The sigma phase at the root of the weld provided selective corrosion, affecting the resistance to pitting corrosion.
- The spray mode generated coarse delta-ferrite and sigma phase in the austenite–ferrite interface, resulting in an extensive micro-region impoverished in Cr and Mo, thus reducing the pitting potential.
- The short-circuit mode generated a refined ferrite due to the slower cooling rate, with the precipitation of the sigma phase inside the delta-ferrite and consequent selective corrosion of such phase, also reducing the pitting potential.
- The weld face of all transfer modes did not generate sigma phase and, consequently, showed the higher corrosion resistance among weld regions.
- The pulsed-arc transfer mode of MAG welding showed, relatively, a more refined ferrite and large austenite bands, with no evidence of the sigma phase, resulting in the best corrosion performance of multi-pass MAG welding of AISI 316L stainless steel.

Conflicts of interest

The authors declare no conflicts of interest.

Acknowledgments

The authors would like to thank the São Paulo Research Foundation (FAPESP) for providing financial support for this research (Proc. no. 2019/23063-4).

REFERENCES

[1] Roberge PR. Handbook of corrosion engineering; 2000, http://dx.doi.org/10.1016/S0026-0576(00)83445-5.
[2] Kurgan N, Varol R. Mechanical properties of P/M 316L stainless steel materials. Powder Technol 2010;201:242–7, http://dx.doi.org/10.1016/j.powtec.2010.03.041.
[3] Rosso M, Porto G, Wood JV. Properties of high density sintered 316L stainless steels. Advances in Powder Metallurgy and Particulate Materials, vol. 5; 1996. Washington, DC; USA; 16–21 June 1996.
[4] Ningshen S, Mudali UK. Pitting and intergranular corrosion resistance of AISI type 301LN stainless steels. J Mater Eng Perform 2010;19:274–81, http://dx.doi.org/10.1007/s11665-009-9441-7.
[5] Saeidi K, Neikter M, Olsen J, Shen ZJ, Akhtar F. 316L stainless steel designed to withstand intermediate temperature. Mater Des 2017;135:1–8, http://dx.doi.org/10.1016/j.matdes.2017.08.072.
[6] Sedriks AJ. Corrosion of stainless steels; 1996.
[7] Scotti A, Ponomarev V, Lucas W. A scientific application oriented classification for metal transfer modes in GMA welding. J Mater Process Technol 2012;212:1406–13, http://dx.doi.org/10.1016/j.jmatprotec.2012.01.021.
[8] Iordachescu D, Quintino L. Steps toward a new classification of metal transfer in gas metal arc welding. J Mater Process Technol 2008;202:391–7, http://dx.doi.org/10.1016/j.jmatprotec.2007.08.081.
[9] Kim YS, Eagar TW. Analysis of metal transfer in gas metal arc welding. Weld J 1993;1:269s–78s, http://dx.doi.org/10.1007/s11663-003-0080-3.
[10] Deng B, Wang Z, Jiang Y, Sun T, Xu J, Li J. Effect of thermal cycles on the corrosion and mechanical properties of UNS S31803 duplex stainless steel. Corros Sci 2009;51:2969–75, http://dx.doi.org/10.1016/j.corsci.2009.08.015.
[11] Tan H, Wang Z, Jiang Y, Yang Y, Deng B, Song H, et al. Influence of welding thermal cycles on microstructure and pitting corrosion resistance of 2304 duplex stainless steels. Corros Sci 2012;55:368–77, http://dx.doi.org/10.1016/j.corsci.2011.10.039.
[12] Kim YH, Lee DJ, Byun JC, Jung KH, Kim JI, Lee HJ, et al. The effect of sigma phases formation depending on Cr/Ni

equivalent ratio in AISI 316L weldments. Mater Des 2011;32:330–6, http://dx.doi.org/10.1016/j.matdes.2010.06.044.
[13] Lippold JC, Kotecki DJ. Welding metallurgy and weldability of stainless steels. John Wiley and Sons Inc.; 2005, http://dx.doi.org/10.1002/9781118960332.
[14] Padilha AF, Rios PR. Decomposition of austenite in austenitic stainless steels. ISIJ Int 2002;42:325–7, http://dx.doi.org/10.2355/isijinternational.42.325.
[15] Hsieh C-C, Wu W. Overview of intermetallic sigma (σ) phase precipitation in stainless steels. ISRN Metall 2012;2012:1–16, http://dx.doi.org/10.5402/2012/732471.
[16] Villanueva DME, Junior FCP, Plaut RL, Padilha AF. Comparative study on sigma phase precipitation of three types of stainless steels: austenitic, superferritic and duplex. Mater Sci Technol 2006;22:1098–104, http://dx.doi.org/10.1179/174328406X109230.
[17] Padilha AF, Escriba DM, Materna-Morris E, Rieth M, Klimenkov M. Precipitation in AISI 316L(N) during creep tests at 550 and 600 °C up to 10 years. J Nucl Mater 2007;362:132–8, http://dx.doi.org/10.1016/j.jnucmat.2006.12.027.
[18] Zingales A, Quartarone G, Moretti G. Sigma phase intergranular corrosion effects in austenitic welds containing ferrite. Corrosion 1985;41:136–41.
[19] Terada M, Escriba DM, Costa I, Materna-Morris E, Padilha AF. Investigation on the intergranular corrosion resistance of the AISI 316L(N) stainless steel after long time creep testing at 600 °C. Mater Charact 2008;59:663–8, http://dx.doi.org/10.1016/j.matchar.2007.05.017.
[20] Magnabosco R, Alonso-Falleiros N. Pit morphology and its relation to microstructure of 850 degrees C aged duplex stainless steel. Corrosion 2005;61:130–6.
[21] Guilherme LH, Della Rovere CA, Kuri SE, de Oliveira MF. Corrosion behaviour of a dissimilar joint TIG weld between austenitic AISI 316L and ferritic AISI 444 stainless steels. Weld Int 2016;30:268–76, http://dx.doi.org/10.1080/09507116.2015.1096476.
[22] Conejero O, Palacios M, Rivera S. Premature corrosion failure of a 316L stainless steel plate due to the presence of sigma phase. Eng Fail Anal 2009;16:699–704, http://dx.doi.org/10.1016/j.engfailanal.2008.06.022.
[23] Cui Y, Lundin CD. Austenite-preferential corrosion attack in 316 austenitic stainless steel weld metals. Mater Des 2007;28:324–8, http://dx.doi.org/10.1016/j.matdes.2005.05.022.
[24] Dadfar M, Fathi MH, Karimzadeh F, Dadfar MR, Saatchi A. Effect of TIG welding on corrosion behavior of 316L stainless steel. Mater Lett 2007;61:2343–6, http://dx.doi.org/10.1016/j.matlet.2006.09.008.
[25] Cui Y, Lundin CD. Evaluation of initial corrosion location in E316L austenitic stainless steel weld metals. Mater Lett 2005;59:1542–6, http://dx.doi.org/10.1016/j.matlet.2005.01.018.
[26] Jang AY, Lee HW. Influence of sigma phase on pitting resistance depending on solidification mode in AISI316l weld metal. Metall Mater Trans A 2012;43:1736–41, http://dx.doi.org/10.1007/s11661-012-1147-z.
[27] Guilherme MF, Rovere LH, Kuri CAD, Oliveira SE. Resistência à corrosão de junta dissimilar soldada pelo processo TIG composta pelos aços inoxidáveis AISI316L e AISI444. Soldag e Insp 2014;19:42–50, http://dx.doi.org/10.1590/S0104-92242014000100006.
[28] Andreatta F, Fedrizzi L. The use of the electrochemical micro-cell for the investigation of corrosion phenomena. Electrochim Acta 2015;203:337–49, http://dx.doi.org/10.1016/j.electacta.2016.01.099.
[29] Abodi LC, Dolgikh O, Terryn H, Deconinck J. The influence of the capillary size and shape on the readings of the electrochemical microcapillary technique: a parametric study by means of the multi-ion modeling. Electrochim Acta 2016;189:128–36, http://dx.doi.org/10.1016/j.electacta.2015.11.068.
[30] Andreatta F, Matesanz L, Akita AH, Paussa L, Fedrizzi L, Fugivara CS, et al. SAE 1045 steel/WC-Co/Ni-Cu-Ni/SAE 1045 steel joints prepared by dynamic diffusion bonding: microelectrochemical studies in 0.6 M NaCl solution. Electrochim Acta 2009;55:551–9, http://dx.doi.org/10.1016/j.electacta.2009.09.025.
[31] Arjmand F, Adriaens A. Microcapillary electrochemical droplet cells: applications in solid-state surface analysis. J Solid State Electrochem 2014;18:1779–88, http://dx.doi.org/10.1007/s10008-014-2413-3.
[32] Andreatta F, Lohrengel MM, Terryn H, De Wit JHW. Electrochemical characterisation of aluminium AA7075-T6 and solution heat treated AA7075 using a micro-capillary cell. Electrochim Acta 2003;48:3239–47, http://dx.doi.org/10.1016/S0013-4686(03)00379-7.
[33] Andreatta F, Terryn H, De Wit JHW. Corrosion behaviour of different tempers of AA7075 aluminium alloy. Electrochim Acta 2004;49:2851–62, http://dx.doi.org/10.1016/j.electacta.2004.01.046.
[34] Suter H, Bohni T. Microelctrodes for corrosion studies in microsystems. Electrochim Acta 2001;47:191–9, http://dx.doi.org/10.1016/S0013-4686(01)00551-5.
[35] Böhni H, Suter T, Assi F. Micro-electrochemical techniques for studies of localized processes on metal surfaces in the nanometer range. Surf Coat Technol 2000;130:80–6, http://dx.doi.org/10.1016/S0257-8972(00)00681-2.
[36] Lohrengel MM, Rosenkranz C, Klüppel I, Moehring A, Bettermann H, Van Den Bossche B, et al. A new microcell or microreactor for material surface investigations at large current densities. Electrochim Acta 2004;49:2863–70, http://dx.doi.org/10.1016/j.electacta.2004.01.068.
[37] Pereda MD, Gervasi CA, Llorente CL, Bilmes PD. Microelectrochemical corrosion study of super martensitic welds in chloride-containing media. Corros Sci 2011;53:3934–41, http://dx.doi.org/10.1016/j.corsci.2011.07.040.
[38] Sánchez M, Gamby J, Perrot H, Rose D, Vivier V. Microelectrochemistry of copper in NaCl solution: comparison between conventional microelectrode and microelectrochemical cell. Electrochem Commun 2010;12:1230–2, http://dx.doi.org/10.1016/j.elecom.2010.06.026.
[39] Garcia C, de Tiedra MP, Blanco Y, Martin O, Martin F. Intergranular corrosion of welded joints of austenitic stainless steels studied by using an electrochemical minicell. Corros Sci 2008;50:2390–7, http://dx.doi.org/10.1016/j.corsci.2008.06.016.
[40] Garcia C, Martin F, de Tiedra P, Blanco Y, Lopez M. Pitting corrosion of welded joints of austenitic stainless steels studied by using an electrochemical minicell. Corros Sci 2008;50:1184–94, http://dx.doi.org/10.1016/j.corsci.2007.11.028.
[41] Martin F, Garcia C, Tiedra P, Blanco Y, Lopez M. Application of minielectrochemical cell to corrosion studies of welded joints of austenitic stainless steel. Corros Eng Sci Technol 2008;43:343–52, http://dx.doi.org/10.1179/174327808X286301.
[42] Mukherjee M, Kumar T. Materials characterization evaluation of microstructural and mechanical properties of Fe-16Cr-1Ni- 9Mn-0. 12N austenitic stainless steel welded joints. Mater Charact 2017;131:406–24, http://dx.doi.org/10.1016/j.matchar.2017.07.028.
[43] ASME IX. Qualification standard for welding, brazing and fusing procedures. In: ASME boiler and pressure vessel code; 2015.

[44] Xue J, Xu M, Huang W, Zhang Z, Wu W, Jin L. Stability and heat input controllability of two different modulations for double-pulse MIG welding. Appl Sci 2019;9:127, http://dx.doi.org/10.3390/app9010127.
[45] Reccagni DL, Guilherme P, Lu LH, Gittos Q, Engelberg M. Reduction of austenite-ferrite galvanic activity in the heat-affected zone of a gleeble-simulated grade 2205 duplex stainless steel weld. Corros Sci 2019;161:108198, http://dx.doi.org/10.1016/j.corsci.2019.108198 [Accepted].
[46] Guilherme LH, Benedetti A, Fugivara C. A portable electrochemical microcell for weld inspection of duplex stainless steel tanks. Corrosion 2018;75:340–8, http://dx.doi.org/10.5006/3004.
[47] Guilherme DL, Reccagni LH, Benedetti P, Fugivara AV, Engelberg CS. Corrosion assessment of ASME qualified welding procedures for grade 2101 lean duplex stainless steel. Corrosion 2019;75:1216–29.